Draft version August 16, 2021
Typeset using LaTeX twocolumn style in AASTeX631

An Imaging Search for Circumstellar Companions of Sirius B

Miles Lucas [1], Michael Bottom [2], Garreth Ruane [3] and Sam Ragland [4]

[1] Institute for Astronomy, University of Hawaii at Manoa, 2680 Woodlawn Dr, Honolulu, HI 96822, USA
[2] Institute for Astronomy, University of Hawaii at Hilo, 640 N Aohoku Pl, Hilo, HI 96720, USA
[3] Jet Propulsion Laboratory, California Institute of Technology, 4800 Oak Grove Dr, Pasadena, CA 91109, USA
[4] W.M. Keck Observatory, 65-1120 Mamalahoa Hwy, Waimea, HI 96743, USA

ABSTRACT

We present deep imaging of Sirius B, the closest and brightest white dwarf. We use Keck/NIRC2 in Lp-band (3.776 µm) across three epochs in 2020 using the technique of angular differential imaging. We reach sub-Jupiter sensitivities and sub-AU separations, reaching $3.5\,\mathrm{M_J}$ at 0.25 AU down to a sensitivity of $0.6\,\mathrm{M_J}$ at 1.5 AU. The uncertainty in mass sensitivity is below $0.1\,\mathrm{M_J}$ due to the precisely known Sirius B system age. Consistent with previous results, we do not detect any companions around Sirius B.

1. INTRODUCTION

High-contrast imaging (HCI) is a powerful technique for discovering and characterizing exoplanets. Probing the architecture, formation, and atmospheres of planets directly is necessary for advancing substellar companion formation and evolution theory. Imaging a planet is challenging, however. The typical astrophysical flux ratios (contrast) for a Sun-Jupiter analog in the near-infrared (NIR) are $\sim 10^{-8}$, and for a Sun-Earth system are $\sim 10^{-10}$ (Traub & Oppenheimer 2010). Thermal emission from exoplanets peaks in the infrared and is well into the Rayleigh-Jeans limit of the star, decreasing contrast compared to the visible or ultraviolet. In addition, the close angular separations of planets make it difficult to detect them over the diffraction pattern of their host and other noise sources.

Typical targets for imaging are nearby young stars; the proximity means the same angular separation probes a smaller physical separation, allowing for studies closer to solar-system scales. Younger exoplanets are hotter and therefore brighter, reducing the flux ratio between the planet and its host star. Another way to reduce contrast would be to image a faint star with bright companions, such as a young white dwarf (WD) star. When intermediate-mass stars ($1\,\mathrm{M_\odot}$ to $8\,\mathrm{M_\odot}$) eventually exit the main-sequence (MS) they expand up to ∼100s of stellar radii during the red giant branch (RGB) phase. This expansion engulfs planets within the star's Roche limit. If the planet survives this expansion, its orbital separation will gradually increase as the star loses mass during the asymptotic giant branch (AGB) phase. Finally, once the star becomes a white dwarf it begins cooling, which will reduce its luminosity by 3 to 4 orders of magnitude compared to its MS progenitor. The faintness, lack of spectral features, and expanded orbits make white dwarfs exceptionally challenging for the transit photometry and radial velocity methods. However, the reduced contrast due to the faintness of the star, and the expanded separation of planets both benefit imaging.

Corresponding author: Miles Lucas
mdlucas@hawaii.edu

2. POST-MS EVOLUTION

There is limited knowledge of planetary systems around evolved stars. Burleigh et al. (2002); Veras (2016) suggest exoplanets on initially wide (>5 AU) orbits around intermediate-mass stars will survive expansion during the RGB phase. Planets very close to the Roche limit of the expanding red giant can still be shredded by tidal forces despite escaping engulfment, although the tidal forces are negligible on planets that are far from the Roche limit (and readily escape engulfment) (Nordhaus & Spiegel 2013). During the AGB phase, stellar mass loss adiabatically expands the orbit of the planet by a maximum factor of $M_{*,\mathrm{MS}}/M_{*,\mathrm{WD}}$ (Jeans 1924). In addition to *first-generation* planets, there are potential methods for *second-generation* planets to form after the violent RGB and AGB phases (Perets 2010).

The first search for substellar companions around white dwarfs was conducted by Probst (1983). They searched for infrared (IR) excess in their spectral energy distributions (SED) using broadband photometry. The IR excess would be indicative of thermal emission of faint material around the star, such as a circumstellar disk or giant planet. They studied ∼100 white dwarfs but found no companions. The same method was applied by Zuckerman & Becklin (1987), who found excess IR emission around white dwarf G29-38. The emission was determined to be from a dust disk (Telesco et al. 1990), which was associated with accretion onto the white dwarf's surface, polluting the stellar atmosphere (Koester et al. 1997). It is estimated that while a third of white dwarfs are polluted, only a few percent have IR excesses (Bonsor & Veras 2015). Skemer & Close (2011) suggested stellar radiation from stars hotter than 15.000 K would sublimate dust, therefore, suppressing any IR excess.

Imaging is well-suited for studying evolved planetary systems, yet to date, only one planet has been imaged around a white dwarf. Luhman et al. (2011) discovered a companion around WD 0806-661B with a mass of $7\,\mathrm{M_J}$ on a wide 2500 AU orbit using Spitzer. The "Degenerate Objects around Degenerate Objects" survey (DODO; Hogan et al. 2009) observed 29 white dwarfs with Gemini/NIRI and VLT/ISAAC, reaching an average upper limit around $\sim 8\,\mathrm{M_J}$ beyond 35 AU. The young white dwarf GD 50 was observed using the extreme AO instrument SPHERE at the VLT (Xu et al. 2015), reaching sensitivity limits of $4\,\mathrm{M_J}$ at 6.2 AU.

3. SIRIUS B AND THE SIRIUS SYSTEM

A particularly fascinating target is Sirius B, the closest and brightest white dwarf. The Sirius system is the 7th closest to the sun at 2.6 pc, consisting of Sirius A, a -1.35 magnitude A1Vm star known for being the brightest, and Sirius B, a DA2 white dwarf with a 50 yr orbit (Bond et al. 2017; Gaia Collaboration et al. 2018). As mentioned previously, the proximity and faintness of Sirius B (compared to a MS star) make it compelling for imaging. Additionally, the young system age (∼225 Myr) means any giant planets would still retain much of their latent formation heat, increasing their luminosity in the IR (Fortney et al. 2010).

A common problem in direct imaging is determining planetary masses from photometry using planetary atmosphere evolution grids. This method of interpolation depends on the stellar age, the stellar photometry, and the distance to the system. Determining stellar ages is quite difficult and sometimes impossible, and is often the largest source of uncertainty when interpolating planetary masses. Age uncertainty exponentially affects young systems (<1 Gyr) due to the rapid cooling of giant planets. Sirius B avoids these pitfalls due to its unusually high age precision, primarily derived from accurate dynamical masses.

The dynamical masses are determined through astrometric studies; the first study of Sirius was performed by Bessel (1844), who recognized wobbles in the proper motion of Sirius A caused by a "dark satellite". This dark satellite was visually confirmed in Bond (1862) as Sirius B. Adams (1915) took the first spectral measurements of Sirius B and found it to be similar to a MS early A-type star, despite its faintness, which we now know to be typical of white dwarf spectra.

Initial astrometric measurements suggested a 50 year orbital period for Sirius B (Auwers 1864). van den Bos (1960); Gatewood & Gatewood (1978) were the first to estimate dynamical masses using compilations of photographic plates from Lick and Yerkes observatories. Bond et al. (2017) greatly refined the orbital solution using a compilation of historical data and Hubble Space Telescope (HST) data, which gave dynamical masses of $(2.063 \pm 0.023)\,\mathrm{M_\odot}$ and $(1.018 \pm 0.011)\,\mathrm{M_\odot}$ for A and B, respectively. A companion around Sirius B would be affected by the orbit of Sirius A, and this constrained three-body system has been studied numerically (Holman & Wiegert 1999). Bond et al. (2017) calculate the longest period stable companion around Sirius B is 1.79 yr, which corresponds to a 1.5 AU circular orbit.

To find the total age of Sirius B, Bond et al. (2017) used isochrones to constrain the cooling age (126 Myr), first. Applying the initial-final mass relation (IFMR) of white dwarfs (Cummings et al. 2016) the estimated progenitor mass of Sirius B is between $5\,\mathrm{M_\odot}$ to $5.6\,\mathrm{M_\odot}$, which, when combined with stellar evolution codes, yielded total system ages between 226 Myr to 228 Myr with an uncertainty of about ±10 Myr (Bond et al. 2017). An age uncertainty of ∼1% is exceptional compared to the ∼10% or worse of stars found in young moving groups, not to mention many stars cannot be precisely dated at all.

The first modern imaging study searching for companions around Sirius B was Schroeder et al. (2000) who used the HST wide-field planetary camera (WFPC) at 1 µm. Around the same time Kuchner & Brown (2000) searched in a narrower field of view (FOV) with HST/NICMOS at 1 µm. These studies combined had a sensitivity down to $\sim 10\,\mathrm{M_J}$ at 5.3 AU (2″). Bonnet-Bidaud & Pantin (2008) used the ground-based ESO/ADONIS instrument in J, H, and Ks-band and reached a sensitivty of $\sim 30\,\mathrm{M_J}$ at 7.9 AU (3″). Skemer & Close (2011) used mid-IR (up to 10 µm) observations from Gemini/T-ReCs which ruled out evidence for any infrared excess around Sirius B. Thalmann et al. (2011) used Subaru/IRCS at 4.05 µm reaching detection sensi-

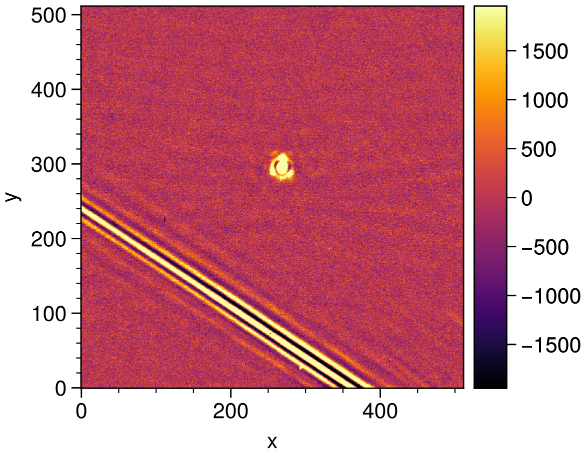

Figure 1. A diffraction spike sweeping across a calibrated science frame of Sirius B from the first epoch. This shows the strong scattered light effects of Sirius A and how they affect the FOV of Sirius B 11″ away.

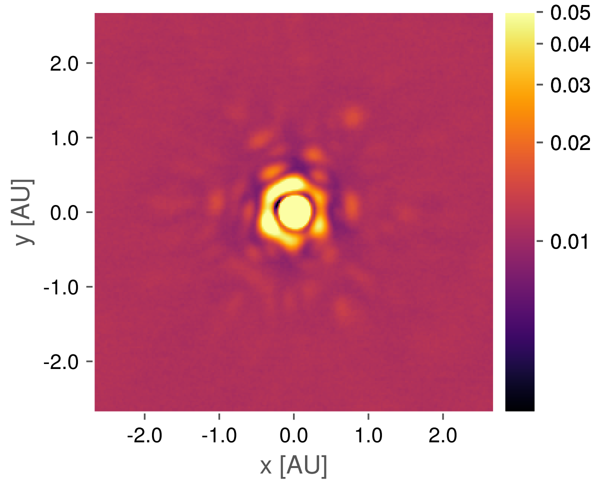

Figure 2. The median frame from the second epoch showing the instrumental PSF. The inner core has a FWHM of ∼76 mas. The speckle pattern is shown in the blobs surrounding the first ring, with roughly 6-way radial symmetry corresponding to the hexagonal shape of the primary mirror.

tivities of 6 M_J to 12 M_J at 1″. Recently, Pathak et al. (2021) took simultaneous mid-IR observations (10 µm) at VLT/VISIR of Sirius A (through a coronagraph) and B. Because of the simultaneous observation, their contrast depended on which region of the FOV was tested. Their average sensitivity is $\sim$2.5 M_J at 1 AU, and their best sensitivity (from the "inner" region) is $\sim$1.5 M_J at 1 AU.

In this work, we report direct images of Sirius B with Keck/NIRC2. The rest of the manuscript is organized as follows: section 4 describes our target and observing strategy, section 5 describes the processing and analysis techniques used, and section 6 describes our results.

4. OBSERVATIONS

Despite Sirius B being the brightest white dwarf in the sky, it is still 10 magnitudes fainter than Sirius A, making it a technically challenging target, especially on ground-based telescopes. We directly imaged Sirius B with Keck/NIRC2 in Lp-band (3.776 µm) using the narrow camera (10 mas px^{-1}; 2.5″×2.5″) across three epochs in 2020 (table 1). Our first attempt to observe Sirius B failed due to the strong scattered light from Sirius A. The adaptive optics (AO) calibration failed when the scattered light from Sirius A would sweep into the FOV of the wavefront sensor (WFS). Similarly, trying to deploy the focal-plane vortex coronagraph (Serabyn et al. 2017) failed when the coronagraphic pointing control algorithm, `QACITS` (Huby et al. 2017), performed erratically in the presence of the scattered light. We did not try coronagraphy for the remaining observations. Vigan et al. (2015, §2) reported similar issues in their attempts to image Sirius B coronagraphically using VLT/SPHERE. In order to overcome these obstacles, we decided to try using Sirius A as the AO guide star and off-axis guiding to Sirius B.

The Keck AO system (Wizinowich et al. 2000) was saturated by Sirius A, so we attenuated the flux using a narrow laser-line filter in the WFS. While still bright (appearing like a $\sim$5 magnitude star on the WFS), this was enough attenuation to close the AO loop. From here, we slewed off-axis using the separations and position angles calculated in table 1 from the orbital parameters in Bond et al. (2017). In this mode, we noticed higher than usual drift in the focal plane, requiring manually recentering the target every 5 or 10 minutes.

During each observation, we took dark frames and sky-flat frames for calibration. All observations were taken with the telescope's field rotator set to track the telescope pupil in order to exploit the natural rotation of the sky via angular differential imaging (ADI; Marois et al. 2006).

5. ANALYSIS

5.1. *Pre-processing*

The raw images from NIRC2 required pre-processing before analyzing them for companions. For each epoch, we applied a flat correction using calibration frames captured during observing. We also removed bad pixels using a combination of `L.A.Cosmic` (van Dokkum 2001) and an adaptive sigma-clipping algorithm. We removed sky background using a high-pass median filter with a

Table 1. Observing parameters for the three epochs of data. All observations were carried out using the NIRC2 narrow camera ($10\,\mathrm{mas\,px^{-1}}$; $2.5'' \times 2.5''$) in Lp-band ($3.776\,\mu\mathrm{m}$). Observation time is based on the frames that were selected for processing. Seeing values were measured at $0.5\,\mu\mathrm{m}$ using a differential image motion monitor (DIMM) and averaged over the observing session. Seeing values, temperature, and water vapor measurements were all taken from the Maunakea weather center forecast archive.

Date observed	Sirius B offset ($''$)	Sirius B PA ($^\circ$)	Obs. time (hr)	FOV rotation ($^\circ$)	FWHM (mas)	Seeing ($''$)	Temp ($^\circ$C)	PWV (mm)
2020-02-04	11.20	67.90	1.44	60.1	79.9	0.936	0.0	0.7
2020-11-21	11.27	66.42	2.91	91.4	76.4	0.871	0.8	3.5
2020-11-28	11.27	66.38	2.44	80.4	82.2	1.23	-1.5	3.0

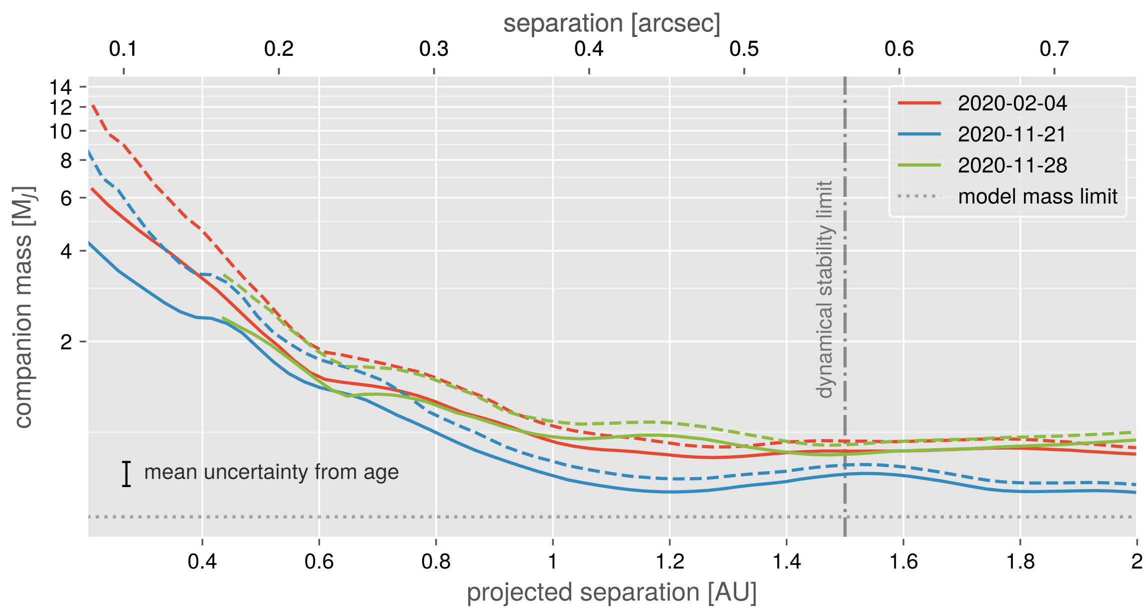

Figure 3. The contrast curves for the best performing algorithm from each epoch. The solid lines are the Gaussian 5σ contrast curves and the dashed lines are the Student-t corrected curves. The mean uncertainty from the total system age ($\sim$10 Myr) is shown by a lone error bar. In addition, the expected upper limit for orbital separation of a stable orbit of 1.5 AU is plotted as a vertical dashed line. The companion mass values are interpolated from the AMES-Cond grid. The lower mass limit (upper magnitude limit) of these models is plotted in a light-gray horizontal dashed line. The annular PCA curve is cut off because the innermost annulus had greater than 1 contrast, which is invalid.

box size of 31 pixels. For both the November epochs we tried exploiting the large focal plane drifts by dithering between two positions in order to simplify background subtraction, but this ended up performing worse than the high-pass filter. At this point frames were manually selected to remove bad frames, especially those with diffraction spikes from Sirius A within a few hundred pixels, like in fig. 1. Then, each good frame was co-registered to sub-pixel accuracy using the algorithm presented in Guizar-Sicairos et al. (2008), followed by fitting each frame with a Gaussian PSF to further increase centroid accuracy.

The co-registered frames were shifted to the center of the FOV and cropped to the inner 200 pixels. With a pixel scale of 10 mas the crop corresponds to a maximum separation of $1''$ or a projected separation of 2.7 AU. All the frames were stacked into data cubes for each epoch. We also measure the parallactic angle of each frame, including corrections for distortion effects following Yelda et al. (2010). For each epoch, we measure the full-width at half-maximum (FWHM) of the stellar PSF for use in post-processing by fitting a bivariate Gaussian model to the median frame from each data cube (fig. 2). All of the pre-processing code is available in Jupyter notebooks in a GitHub repository (https://github.com/mileslucas/sirius-b) and the pre-processed data cubes and parallactic angles are available on Zenodo: 10.5281/zenodo.5115225.

5.2. *Post-processing*

By taking data with the field rotator disabled (ADI), the point-spread function (PSF) will not appear to rotate while any potential companion will appear to rotate. This reduces the probability of removing companion signal when we subtract the stellar PSF model. After subtraction, the frames are derotated by their parallactic angle and combined with a weighted sum (Bottom et al. 2017), which reduces the pixel-to-pixel noise as the number of frames in the data cube increases.

For this analysis, we used four ADI algorithms for modeling and subtracting the stellar PSF: median subtraction (Marois et al. 2006), principal component analysis (PCA, also referred to as KLIP; Soummer et al. 2012), non-negative matrix factorization (NMF; Ren et al. 2018), and fixed-point greedy disk subtraction (GreeDS; Pairet et al. 2019b, 2020). The median subtraction and PCA methods were also applied in an annular method, where we modeled the PSF in annuli of increasing separation, discarding frames that have not rotated at least 0.5 FWHM (Marois et al. 2006).

We used three metrics to determine the performance of each algorithm, the signal-to-noise ratio (S/N) significance map, the standardized trajectory intensity mean map (STIM map; Pairet et al. 2019a), and the contrast curve. The significance and STIM maps assign a likelihood to each pixel for the presence of a companion using different assumptions of the residual statistics. The contrast curve determines the sensitivity of a 5σ statistical detection through repeated injection and retrieval of planetary signal as processed by one of the ADI algorithms above. We calculate both the Gaussian contrast and the Student-t corrected contrast, which accounts for the small-sample statistics in each annulus (Mawet et al. 2014). The collapsed residual frames along with the above metrics for each algorithm for each epoch are in section A.

A common problem when using subspace-driven post-processing algorithms like PCA, NMF, or GreeDS is choosing the size of the subspace (i.e., the number of components). For PCA, NMF, and GreeDS algorithms, we increased the number of components from 1 to 10, creating a residual cube for each iteration. We chose 10 for the maximum number of components because we saw a dramatic decline in contrast sensitivity after the first few components (fig. 12). In our analysis we employed the STIM largest intensity mask map (SLIM map; Pairet 2020) as an ensemble statistic. The SLIM map calculates the average STIM map from many residual cubes along with the average mask of the N most intense pixels in each STIM map. A real companion ought to be present in many different residual cubes from the same dataset, so this ensemble approach can give us a probability map without predetermining the number of components. The collapsed residual frames, average STIM map, SLIM map, and contrast curves for each epoch for each of the above algorithms are in section A.

All of the ADI algorithms and metrics are implemented in the open-source Julia package `ADI.jl` (Lucas & Bottom 2020). All of the code for the ADI processing in this paper, including the scripts for each figure produced are in a GitHub repository in Jupyter notebooks and Julia scripts (https://github.com/mileslucas/sirius-b).

6. RESULTS

We determined the best-performing algorithms for each epoch using the contrast curves described in section 5. For the first two epochs, full-frame median subtraction had the best contrast at almost all separations. For the last epoch annular PCA subtraction with 2 principal components and a rotation threshold of 0.5 FWHM produced the best contrast at close separations ($0.2''$ to $0.4''$) and had similar performance to other algorithms beyond $0.4''$. The innermost annulus from this algorithm has invalid contrast (>1) and is not shown. The collapsed residual frames from each epoch are shown in fig. 4, along with the Gaussian significance maps (fig. 5) and STIM maps (fig. 6).

The reduced images do not show consistent or significant evidence for a substellar companion. The STIM probability maps for the 2020-11-21 and 2020-11-28 epochs suggest evidence for some blobs $\sim$0.3 AU ($0.13''$; 1.6 FWHM) from the center. The February epoch also shows a blob at a similar separation in the reduced image which does not appear in the STIM map. The lack of statistical evidence in the February epoch and the significance maps as well as the proximity to the central star both reduce the probability of these blobs being true companions. Nonetheless, we estimated astrometry for blobs from each epoch (table 2) and tried fitting Keplerian orbits using the "Orbits for the Impatient" algorithm (OFTI; Blunt et al. 2017). We generated 10^4 orbits, none of which contained the points from each epoch (section B). We take this as direct evidence against the blobs being substellar companions of any kind.

It is interesting to note the morphology of the innermost $\sim 0.4''$ in the frames produced by GreeDS and NMF. Both of these algorithms usually outperform traditional median and PCA subtraction for disk imaging. In the frames from each epoch, but particularly in the two November epochs, a symmetric "barbell" shape can be seen which is similar to other disk images (e.g., fig. 7 Norris et al. 2014). Due to the nature of high-contrast

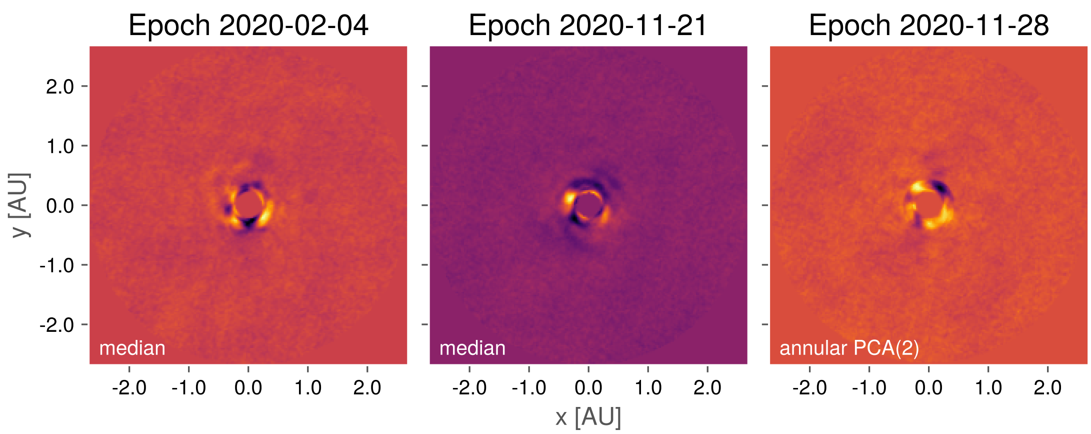

Figure 4. The flat residuals of each epoch after PSF subtraction, derotating, and collapsing. The inner full-width at half-maximum (FWHM) is masked out for each frame.

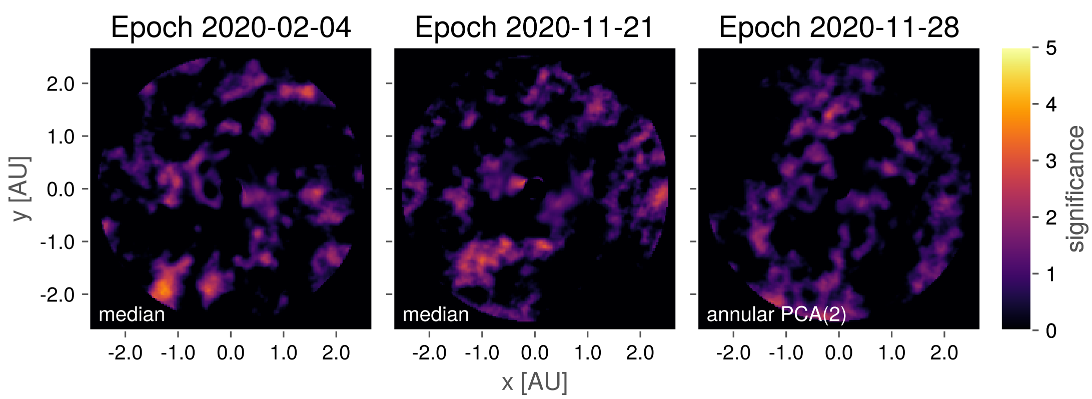

Figure 5. The *significance* maps for each epoch accounting for small-sample statistics (Mawet et al. 2014). Typically a critical value for detection is 5. The inner full-width at half-maximum (FWHM) is masked out for each map.

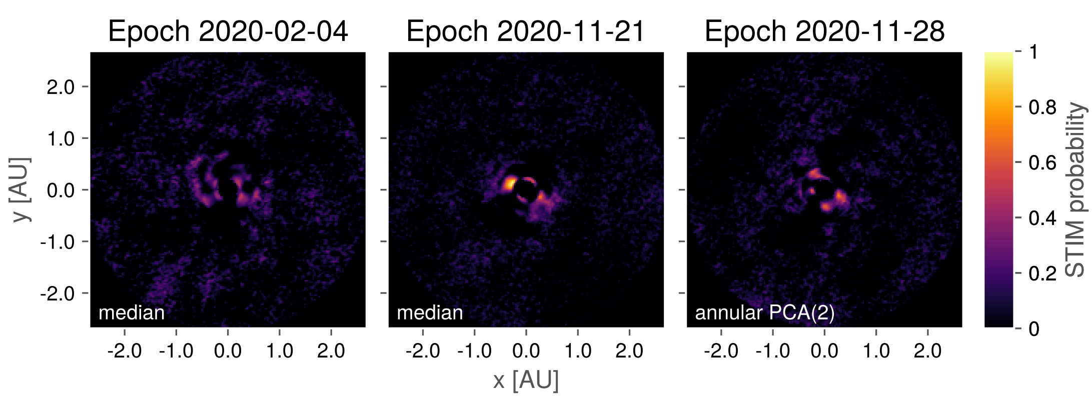

Figure 6. The STIM maps for each epoch calculated from each residual cube. The STIM probability has a typical cutoff threshold of 0.5 for significant detections. The inner full-width at half-maximum (FWHM) is masked out for each map.

imaging, it is difficult to differentiate systematic noise from real signal in the speckle-limited regime, in addition, there is no prior evidence for a circumstellar disk from IR excess. Follow-up work in the visible (e.g., Subaru/VAMPIRES, VLT/ZIMPOL) may be able to image such a disk.

The contrast maps from the best performing algorithm for each reduction are shown in fig. 3. We determine the limiting sensitivities in terms of the planetary mass by first calculating the contrast-limited magnitude using an Lp-band magnitude for Sirius B of 9.1 (adapted from Bonnet-Bidaud & Pantin 2008). Then we used 225 Myr for the system age to interpolate the planetary mass using the AMES-Cond evolutionary grid and atmosphere models (Allard et al. 2012). The high precision of the Sirius system's age reduces uncertainty when interpolating planetary mass from the evolutionary grids (see section 1). We also tested using the newer SONORA grid (Marley et al. 2018; Marley et al. 2021), but the differences compared to AMES-Cond were less than the mean uncertainty from age. The best performing epoch was on the night of 2020-11-21, which managed to reach an exceptional sensitivity of $3.5\,\mathrm{M_J}$ at 0.25 AU ($0.09''$) in the speckle limited regime and ultimately $0.6\,\mathrm{M_J}$ at 1.5 AU ($0.38''$) in the background limited regime.

7. CONCLUSIONS

In closing, the Sirius system is one of the most well studied in history, with Sirius B being the target of companion searches from the visible to the IR. While it is highly unlikely a first-generation planet survived post-MS evolution, imaging efforts have gradually increased the sensitivity to second-generation planets. In this work, we present high-contrast images of Sirius B in the near-IR. Our sensitivity limits are the best that have been reached for Sirius B so far, reaching $0.6\,\mathrm{M_J}$ at 1.5 AU, the outer limit for dynamically stable orbits. Our observations also show how the high precision of the parameters of the Sirius system directly benefits the sensitivity to planets. Particularly, the low age uncertainty of Sirius B keeps our mass uncertainty below $0.1\,\mathrm{M_J}$. Despite the high sensitivity of this study, we found no appreciable evidence for a companion around Sirius B, consistent with previous results. This non-detection furthers evidence against a second-generation planet migrating or forming within the Sirius system (Vigan et al. 2015).

For future work, we consider two avenues for followup. As mentioned in section 6, optical observations using an instrument like Subaru/VAMPIRES (Norris et al. 2014) or VLT/ZIMPOL (Schmid et al. 2018). Optical observations can look for disks in the Rayleigh-scattering regime, which is not readily probed by IR observations. Furthermore, the polarimetric differential observation modes of both instruments allow for nearly diffraction-limited imaging, down to 10s of milliarcseconds.

Followup in the IR from space-based telescopes would increase the sensitivity of the observations due to the absence of background emission from Earth's atmosphere. For example, using JWST/NIRCAM in long-wavelength imaging mode has a limiting magnitude of $\sim$25 in the F480M filter, which would easily reach the model mass sensitivity limits at $>0.3''$ without saturation (Pontoppidan et al. 2016). The pixel scale ($0.06\,''\,\mathrm{px}^{-1}$) and PSF size ($\sim 0.3''$) would still probe down to 0.8 AU. Observations would be complicated by the scattered light from Sirius A, which could affect the fine-pointing control or worsen the background sensitivity. In the end, our ground-based observations are already quite close to the atmospheric model grid limits, raising the concern of diminishing returns. Planetary atmosphere models must improve, before fully reaping the benefits of the additional sensitivity of space-based observations.

We have published alongside this work the entire codebase used for pre-processing and reducing the data, and for generating every figure in this manuscript. We have also published our reduced datasets under an open license. We hope that this improves the reproducibility of the work as well as providing data for testing new ADI algorithms.

ACKNOWLEDGMENTS

The data presented herein were obtained at the W. M. Keck Observatory, which is operated as a scientific partnership among the California Institute of Technology, the University of California, and the National Aeronautics and Space Administration. The Observatory was made possible by the generous financial support of the W. M. Keck Foundation. The authors wish to recognize and acknowledge the very significant cultural role and reverence that the summit of Maunakea has always had within the indigenous Hawaiian community. We are most fortunate to have the opportunity to conduct observations from this mountain.

Facility: Keck:II (NIRC2)

Software: ADI.jl (Lucas & Bottom 2020), astropy (Collaboration et al. 2013; Astropy Collaboration et al. 2018), Julia (Bezanson et al. 2017), numpy (Harris et al. 2020), scikit-image (Walt et al. 2014),

REFERENCES

Adams, W. S. 1915, Publications of the Astronomical Society of the Pacific, 27, 236, doi: 10.1086/122440

Allard, F., Homeier, D., & Freytag, B. 2012, Philos Trans A Math Phys Eng Sci, 370, 2765, doi: 10.1098/rsta.2011.0269

Astropy Collaboration, Price-Whelan, A. M., Sipőcz, B. M., et al. 2018, The Astronomical Journal, 156, 123, doi: 10.3847/1538-3881/aabc4f

Auwers, A. 1864, Monthly Notices of the Royal Astronomical Society, 25, 38. https://ui.adsabs.harvard.edu/abs/1864MNRAS..25...38A

Bessel, F. W. 1844, Monthly Notices of the Royal Astronomical Society, 6, 136, doi: 10.1093/mnras/6.11.136

Bezanson, J., Edelman, A., Karpinski, S., & Shah, V. B. 2017, SIAM Rev., 59, 65, doi: 10.1137/141000671

Blunt, S., Nielsen, E. L., De Rosa, R. J., et al. 2017, The Astronomical Journal, 153, 229, doi: 10.3847/1538-3881/aa6930

Bond, G. 1862, Astronomische Nachrichten, 57, 131. https://ui.adsabs.harvard.edu/abs/1862AN.....57..131B

Bond, H. E., Schaefer, G. H., Gilliland, R. L., et al. 2017, The Astrophysical Journal, 840, 70, doi: 10.3847/1538-4357/aa6af8

Bonnet-Bidaud, J.-M., & Pantin, E. 2008, A&A, 489, 651, doi: 10.1051/0004-6361:20078937

Bonsor, A., & Veras, D. 2015, MNRAS, 454, 53, doi: 10.1093/mnras/stv1913

Bottom, M., Ruane, G., & Mawet, D. 2017, Research Notes of the American Astronomical Society, 1, 30, doi: 10.3847/2515-5172/aa9d18

Burleigh, M. R., Clarke, F. J., & Hodgkin, S. T. 2002, Monthly Notices of the Royal Astronomical Society, 331, L41, doi: 10.1046/j.1365-8711.2002.05417.x

Collaboration, A., Robitaille, T. P., Tollerud, E. J., et al. 2013, Astronomy and Astrophysics, 558, A33, doi: 10.1051/0004-6361/201322068

Cummings, J. D., Kalirai, J. S., Tremblay, P. E., & Ramirez-Ruiz, E. 2016, The Astrophysical Journal, 818, 84, doi: 10.3847/0004-637X/818/1/84

Fortney, J. J., Baraffe, I., & Militzer, B. 2010, Giant Planet Interior Structure and Thermal Evolution. https://ui.adsabs.harvard.edu/abs/2010exop.book..397F

Gaia Collaboration, Brown, A. G. A., Vallenari, A., et al. 2018, Astronomy & Astrophysics, Volume 616, id.A1, <NUMPAGES>22</NUMPAGES> pp., 616, A1, doi: 10.1051/0004-6361/201833051

Gatewood, G. D., & Gatewood, C. V. 1978, The Astrophysical Journal, 225, 191, doi: 10.1086/156480

Guizar-Sicairos, M., Thurman, S. T., & Fienup, J. R. 2008, Opt. Lett., OL, 33, 156, doi: 10.1364/OL.33.000156

Harris, C. R., Millman, K. J., van der Walt, S. J., et al. 2020, Nature, 585, 357, doi: 10.1038/s41586-020-2649-2

Hogan, E., Burleigh, M. R., & Clarke, F. J. 2009, Monthly Notices of the Royal Astronomical Society, 396, 2074, doi: 10.1111/j.1365-2966.2009.14565.x

Holman, M. J., & Wiegert, P. A. 1999, The Astronomical Journal, 117, 621, doi: 10.1086/300695

Huby, E., Baudoz, P., Mawet, D., & Absil, O. 2017, The Astronomical Journal, 153, 43, doi: 10.3847/1538-3881/153/1/43

Jeans, J. H. 1924, Monthly Notices of the Royal Astronomical Society, 85, 2, doi: 10.1093/mnras/85.1.2

Koester, D., Provencal, J., & Shipman, H. L. 1997, Astronomy and Astrophysics, v.320, p.L57-L59, 320, L57. https://ui.adsabs.harvard.edu/abs/1997A%26A...320L..57K/abstract

Kuchner, M. J., & Brown, M. E. 2000, Publications of the Astronomical Society of the Pacific, 112, 827, doi: 10.1086/316581

Lucas, M., & Bottom, M. 2020, Journal of Open Source Software, 5, 2843, doi: 10.21105/joss.02843

Luhman, K. L., Burgasser, A. J., & Bochanski, J. J. 2011, The Astrophysical Journal, 730, L9, doi: 10.1088/2041-8205/730/1/L9

Marley, M., Saumon, D., Morley, C., & Fortney, J. 2018, Sonora 2018: Cloud-free, solar composition, solar C/O substellar atmosphere models and spectra, nc_m+0.0_co1.0_v1.0, Zenodo, doi: 10.5281/zenodo.1309035

Marley, M. S., Saumon, D., Visscher, C., et al. 2021, arXiv e-prints, arXiv:2107.07434. https://arxiv.org/abs/2107.07434

Marois, C., Lafrenière, D., Doyon, R., Macintosh, B., & Nadeau, D. 2006, The Astrophysical Journal, 641, 556, doi: 10.1086/500401

Mawet, D., Milli, J., Wahhaj, Z., et al. 2014, ApJ, 792, 97, doi: 10.1088/0004-637X/792/2/97

Nordhaus, J., & Spiegel, D. S. 2013, Monthly Notices of the Royal Astronomical Society, 432, 500, doi: 10.1093/mnras/stt569

Norris, B., Tuthill, P., Jovanovic, N., et al. 2014, arXiv e-prints, arXiv:1405.7426. https://ui.adsabs.harvard.edu/abs/2014arXiv1405.7426N

Pairet, B. 2020, PhD thesis, UCL - Université Catholique de Louvain. https://dial.uclouvain.be/pr/boreal/object/boreal:240621

Pairet, B., Cantalloube, F., Gomez Gonzalez, C. A., Absil, O., & Jacques, L. 2019a, Monthly Notices of the Royal Astronomical Society, 487, 2262, doi: 10.1093/mnras/stz1350

Pairet, B., Cantalloube, F., & Jacques, L. 2019b, arXiv:1812.01333 [astro-ph]. http://arxiv.org/abs/1812.01333

—. 2020, arXiv:2008.05170 [astro-ph]. http://arxiv.org/abs/2008.05170

Pathak, P., de la Roche, D. J. M. P. d., Kasper, M., et al. 2021, arXiv:2104.13032 [astro-ph]. http://arxiv.org/abs/2104.13032

Perets, H. B. 2010, arXiv e-prints, arXiv:1001.0581. https://ui.adsabs.harvard.edu/abs/2010arXiv1001.0581P

Pontoppidan, K. M., Pickering, T. E., Laidler, V. G., et al. 2016, in Society of Photo-Optical Instrumentation Engineers (SPIE) Conference Series, Vol. 9910, Observatory Operations: Strategies, Processes, and Systems VI, ed. A. B. Peck, R. L. Seaman, & C. R. Benn, 991016, doi: 10.1117/12.2231768

Probst, R. G. 1983, The Astrophysical Journal Supplement Series, 53, 335, doi: 10.1086/190893

Ren, B., Pueyo, L., Zhu, G. B., Debes, J., & Duchêne, G. 2018, The Astrophysical Journal, 852, 104, doi: 10.3847/1538-4357/aaa1f2

Schmid, H. M., Bazzon, A., Roelfsema, R., et al. 2018, A&A, 619, A9, doi: 10.1051/0004-6361/201833620

Schroeder, D. J., Golimowski, D. A., Brukardt, R. A., et al. 2000, The Astronomical Journal, 119, 906, doi: 10.1086/301227

Serabyn, E., Huby, E., Matthews, K., et al. 2017, The Astronomical Journal, 153, 43, doi: 10.3847/1538-3881/153/1/43

Skemer, A. J., & Close, L. M. 2011, The Astrophysical Journal, 730, 53, doi: 10.1088/0004-637X/730/1/53

Soummer, R., Pueyo, L., & Larkin, J. 2012, The Astrophysical Journal Letters, 755, L28, doi: 10.1088/2041-8205/755/2/L28

Telesco, C. M., Joy, M., & Sisk, C. 1990, The Astrophysical Journal, 358, L17, doi: 10.1086/185769

Thalmann, C., Usuda, T., Kenworthy, M., et al. 2011, The Astrophysical Journal, 732, L34, doi: 10.1088/2041-8205/732/2/L34

Traub, W. A., & Oppenheimer, B. R. 2010, Exoplanets, 111. http://adsabs.harvard.edu/abs/2010exop.book..111T

van den Bos, W. H. 1960, Journal des Observateurs, 43, 145. https://ui.adsabs.harvard.edu/abs/1960JO.....43..145V

van Dokkum, P. G. 2001, Publications of the Astronomical Society of the Pacific, 113, 1420, doi: 10.1086/323894

Veras, D. 2016, Royal Society Open Science, 3, 150571, doi: 10.1098/rsos.150571

Vigan, A., Gry, C., Salter, G., et al. 2015, Monthly Notices of the Royal Astronomical Society, 454, 129, doi: 10.1093/mnras/stv1928

Walt, S. v. d., Schönberger, J. L., Nunez-Iglesias, J., et al. 2014, PeerJ, 2, e453, doi: 10.7717/peerj.453

Wizinowich, P. L., Acton, D. S., Lai, O., et al. 2000, 4007, 2, doi: 10.1117/12.390368

Xu, S., Ertel, S., Wahhaj, Z., et al. 2015, Astronomy & Astrophysics, Volume 579, id.L8, <NUMPAGES>5</NUMPAGES> pp., 579, L8, doi: 10.1051/0004-6361/201526179

Yelda, S., Lu, J. R., Ghez, A. M., et al. 2010, The Astrophysical Journal, Volume 725, Issue 1, pp. 331-352 (2010)., 725, 331, doi: 10.1088/0004-637X/725/1/331

Zuckerman, B., & Becklin, E. E. 1987, Nature, 330, 138, doi: 10.1038/330138a0

APPENDIX

A. ADI PROCESSING RESULTS

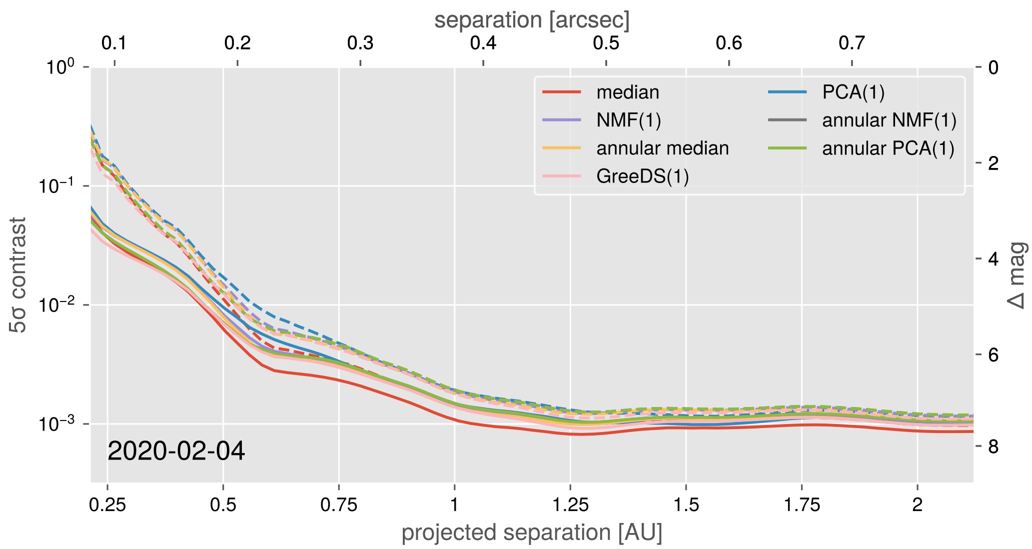

Figure 7. 5σ contrast curves from every ADI algorithm for the first epoch. Both the Gaussian (solid lines) and Student-t corrected (dashed lines) contrast curves are shown.

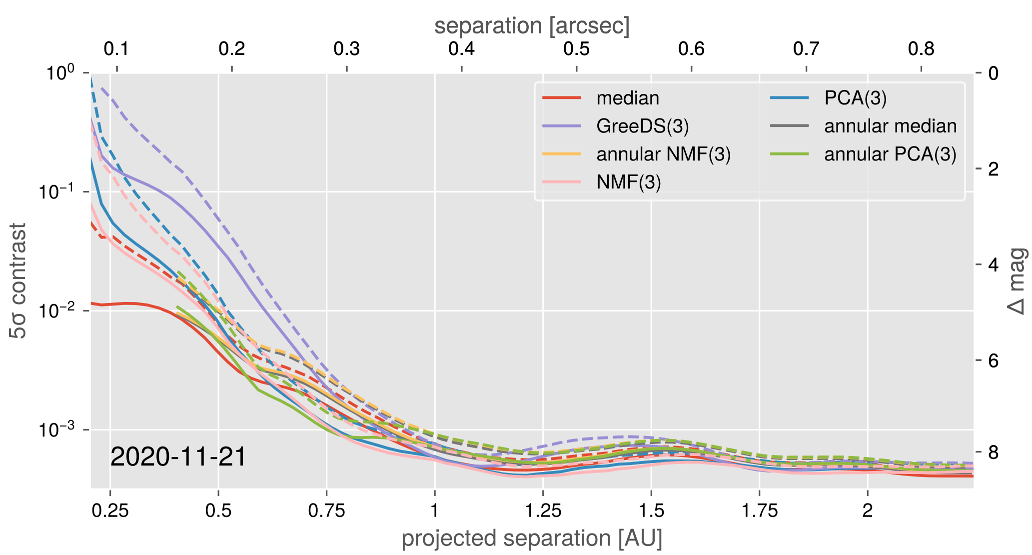

Figure 8. 5σ contrast curves from every ADI algorithm for the second epoch. Both the Gaussian (solid lines) and Student-t corrected (dashed lines) contrast curves are shown.

Fig. Set 10. ADI processing results

Fig. Set 11. PCA, NMF, and GreeDS mosaics

Fig. Set 12. PCA, NMF, and GreeDS results

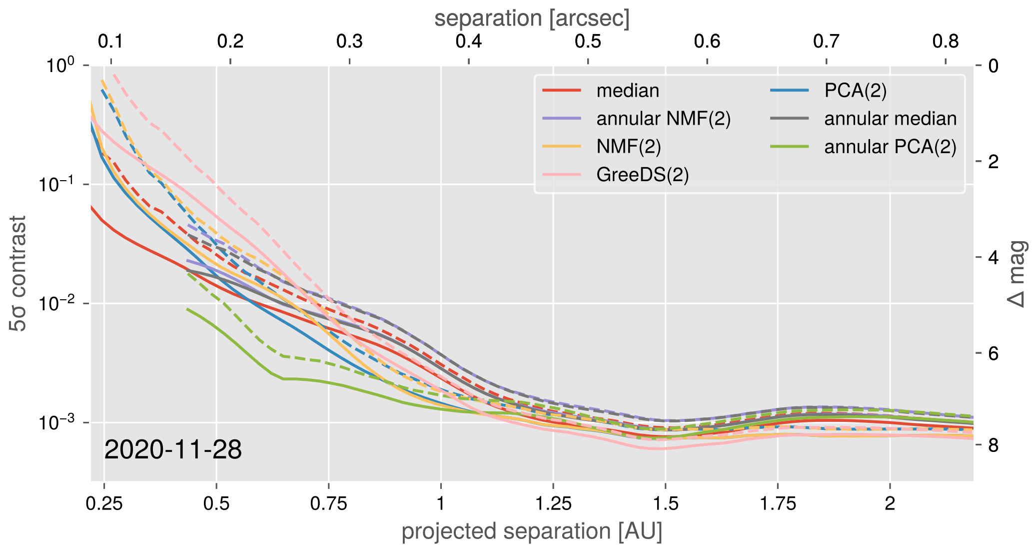

Figure 9. 5σ contrast curves from every ADI algorithm for the third epoch. Both the Gaussian (solid lines) and Student-t corrected (dashed lines) contrast curves are shown.

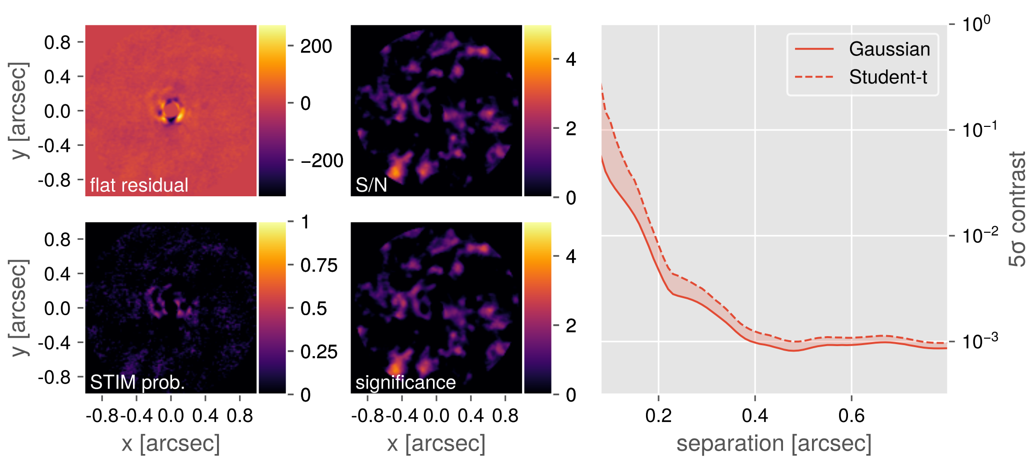

Figure 10. Post-processing results from the second epoch using full-frame median subtraction. The top-left frame is the collapsed residual frame, the top-right is the Gaussian S/N map, the bottom-left is the STIM probability map, and the bottom-right is the Student-t corrected significance map. In each frame the inner FWHM is masked out. The right figure show the Gaussian (solid line) and Student-t corrected (dashed curve) 5σ contrast curve. Outputs for other epochs and other algorithms (21 figures) are in the online figure set and the GitHub repository.

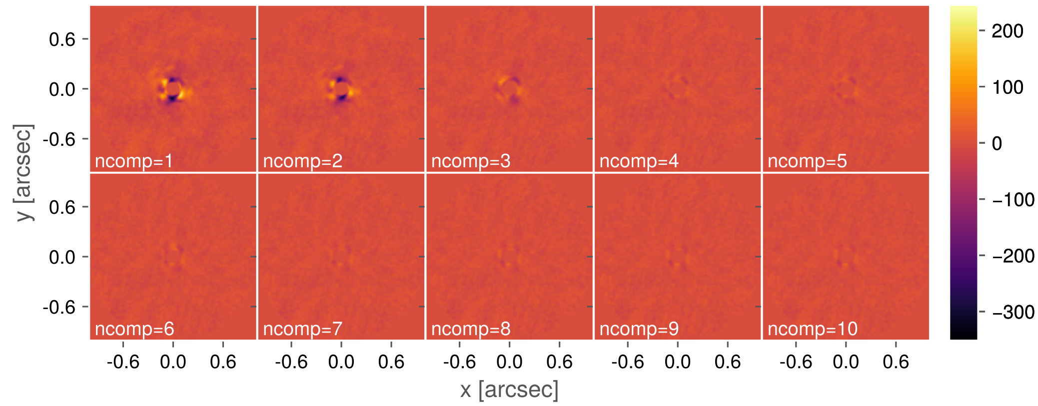

Figure 11. Collapsed residual frames from the first epoch using PCA reduction with 1-10 components. The figures share a common scale and the inner FWHM is masked out for all the frames. Outputs for the other epochs and for the NMF and GreeDS algorithms (9 figures) are in the online figure set and the GitHub repository

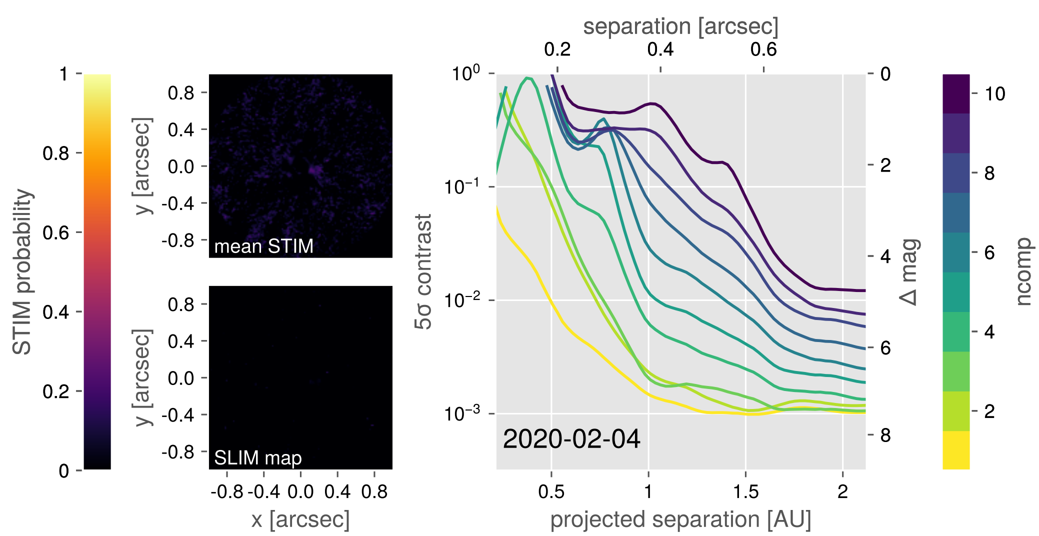

Figure 12. 5σ Gaussian contrast curves for the first epoch using PCA reduction with 1-10 components. The left two figures are the average STIM probability map, and the SLIM detection map. For both of these maps, a typical cutoff value is 0.5. Outputs for the other epochs and for the NMF and GreeDS algorithms (9 figures) are in the online figure set and the GitHub repository.

B. PROVISIONAL ORBIT FITTING

We found multiple interesting blobs in the reduced data that were not statistically significant. Nonetheless, we tried fitting Keplerian orbits using OFTI to determine the feasibility of the blobs being real companions. We began by estimating the astrometry of the blobs by eye in reduced data (table 2, fig. 13). We tried simulating 10^4 orbits via rejection sampling with OFTI but no generated orbit was able to constrain all three points. Overall we determine these blobs are not real companions and are most likely systematic noise in the stellar PSF.

Table 2. Provisional astrometry for a blob of interest from each epoch. The separation and offset are in relation to Sirius B. The uncertainties are derived from the FWHM of the PSF from each epoch.

Date observed	offset (mas)	PA (°)
2020-02-04	123 ± 40	-128 ± 20
2020-11-21	119 ± 38	68 ± 18
2020-11-28	132 ± 41	37 ± 21

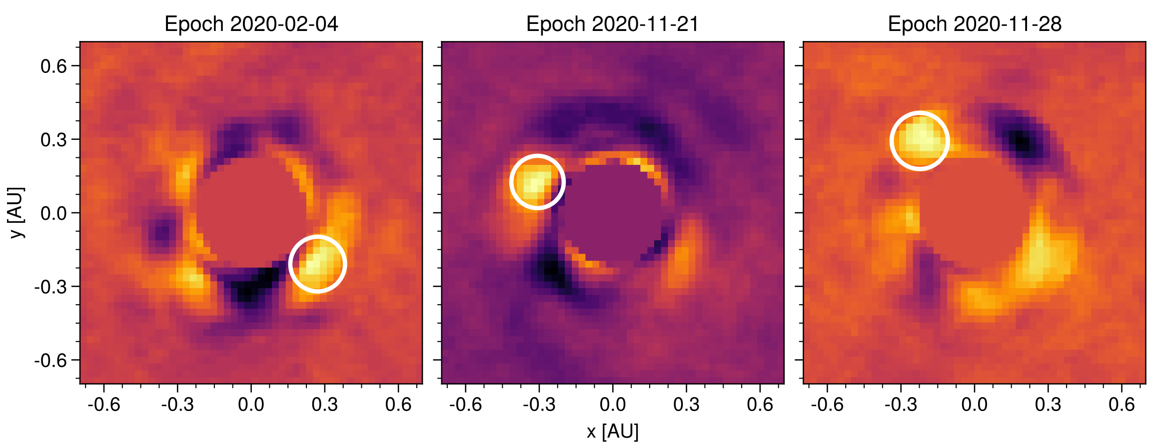

Figure 13. Provisional astrometry (white circles) displayed on collapsed and derotated residuals from each epoch. Each frame was cropped to the inner ∼7 AU (0.25″) and the inner FWHM has been masked out. The width of the circles represents the uncertainty.